Eccentric Tube Robots as Multiarmed Steerable Sheaths

Jiaole Wang ⬡ , *Member, IEEE*, Joseph Peine, and Pierre E. Dupont ⬡ , *Fellow, IEEE*

Abstract—This article presents a novel continuum robot sheath for use in single-port minimally invasive procedures such as neuroendoscopy in which the sheath is designed to deliver multiple robotic arms. Actuation of the sheath is achieved by using precurved superelastic tubes lining the working channels used for arm delivery. These tubes perform a similar role to push/pull tendons, but can accomplish shape change of the sheath via rotation. A kinematic model using Cosserat rod theory is derived, which is based on modeling the system as a set of eccentrically aligned precurved tubes constrained along their length by an elastic backbone. The specific case of a two-arm sheath is considered in detail. Simulation and experiments are used to investigate and validate the concept and model.

Index Terms—Concentric tube robots, multiple arms, steerable sheath.

I. INTRODUCTION

COMPARED to multiport minimally invasive surgeries, single-port endoscopic procedures offer a number of advantages to the patient. These include reduced pain due to fewer incisions and hemorrhaging, and shorter recovery time. In neurosurgery, endoscopy enables navigation through the clear fluid-filled ventricular system of the brain instead of through healthy brain tissue enabling minimally invasive treatment of tumors [1]–[4], cysts [5]–[7], hydrocephalus [8], [9], and epileptogenic lesions [10]. Twenty percent of brain tumors lie either adjacent to, or inside, the ventricles, and endoscopy has had a major impact in their treatment leading to reductions in morbidity and procedure time [11], [12].

A major challenge is that many neuroendoscopes include a single working channel, forcing clinicians to perform one-handed surgery. This approach requires substantial training,

Jiaole Wang is with the School of Mechanical Engineering and Automation, Harbin Institute of Technology, Shenzhen 518055, China. He was with the Department of Cardiovascular Surgery, Boston Children's Hospital, Harvard Medical School, Boston, MA 02115 USA (e-mail: wangjiaole@hit.edu.cn).

Joseph Peine and Pierre E. Dupont are with the Department of Cardiovascular Surgery, Boston Children's Hospital, Harvard Medical School, Boston, MA 02115 USA (e-mail: Joseph.Peine@childrens.harvard.edu; Pierre.Dupont@childrens.harvard.edu).
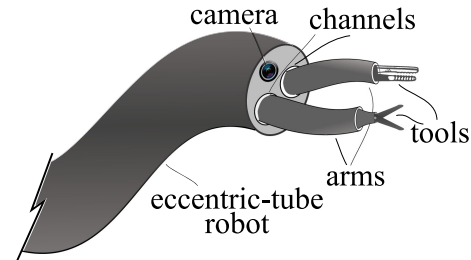
Fig. 1. Conceptual design of a 2-channel eccentric tube robot with two arms delivered through the channels. The channels, which are made from precurved tubes, are designed to act as delivery channels and driving elements simultaneously. Different combinations of tube rotation at proximal ends will results in different sheath shapes and end-effector poses.

leads to longer procedure times, and limits the types of procedures that can be performed. While some rigid endoscopes do allow simultaneous use of two tools, the tools are mounted on straight parallel shafts making it difficult to perform critical tasks like hemostasis. Furthermore, orienting the endoscope tip with respect to the lesion is also challenging and while manual flexible endoscopes provide some steerability, they provide a single working channel and their curvature can make tool control difficult.

A single-port robotic system, as shown in Fig. 1, can address these challenges by providing two or more actuated arms deployed from a steerable endoscopic sheath. While a variety of systems of this type have been developed [13], the sheath diameter of these devices is too large for neurosurgery as well as for other types of procedures. This has led, for example, to the creation of systems in which multiple uncoupled robot arms are introduced to the surgical site [14]. Uncoupled bimanual systems can be more difficult to control, however, and the need for careful arm and sheath design to achieve the necessary surgical workspace has been recognized and is being investigated [15]. Miniaturization in sheath design remains an open challenge with the goal to provide sufficient cross section in the sheath for the arm working channels and optics while also enabling steerable control of the sheath.

Several continuum robot technologies are available to produce a steerable sheath. These include those that use tendons attached to the distal end of a central backbone to cause deflection by pulling [16]. Similarly, tubes can be used instead of tendons to enable both pulling and pushing [17]–[19]. Interlaced continuum robots have also been developed that provide the capabilities of shape locking and follow-the-leader insertion [20], [21]. The latter [21] is currently being commercialized delivering multiple

arms for medical interventions. A sheath could also be constructed as a concentric tube robot [22]–[25]. In particular, the work in [24] proposes a concentric tube sheath for delivering three concentric tube arms.

Since the maximum curvature of concentric tube robots is inversely proportional to their overall diameter, however, tendon/tube designs provide relatively higher curvatures than concentric tube robots as diameter increases. Nevertheless, reducing sheath diameter while preserving arm working-channel diameters and also accommodating the stiffness of the arms passing through the sheath poses limits on what can be achieved with tendons and tubes.

While the arm working channels are typically viewed as passive lumens, this article explores an alternative approach to sheath steering in which precurved superelastic tubes lining the working channels for the arms are used to produce sheath deflection. While actuation could include both rotating and translating these precurved tubes with respect to the sheath, the case of pure rotation is considered here. Since the arm diameters are typically at least a factor of 2 smaller than the sheath diameter, the maximum precurvature of these tubes is proportionally larger than what could be achieved with a sheath constructed from concentric tubes as in [24]. We do note that since the work in [24] considers the elastic interaction between a concentric tube sheath and eccentrically located concentric tube arms passing through the sheath, the kinematic modeling has some similarities. Differences, however, include discrete versus continuous coupling of the working channels/arms to the sheath and our inclusion of the sliding with respect to the arc length that occurs in any eccentric arrangement of curved rods.

The contribution of this article is to model and characterize the capabilities of a sheath whose shape is controlled by the rotation of precurved tubes lining its working channels. It builds on the initial results presented in [26] in several ways. First, it expands the kinematic modeling to consider designs comprised of multiple steerable sections. Second, it presents an improved solution strategy for the kinematics in which the arms and backbones are integrated simultaneously. Third, it explores through simulation and experiment the dependence of elastic stability on design parameters. Finally, it presents model calibration results for single-stage and two-stage experimental prototypes.

The rest of article is organized as follows. Section II presents the steerable sheath architecture for two arm channels. Section III develops a mechanics-based kinematic model for an arbitrary number of arms and sections. It also presents an optimization-based solution technique for the model. The effect of the disk number of sheath shape is investigated in Section IV. Robot workspace and sheath twisting are described in Section V. Elastic stability is considered in Section VI. Section VII presents experimental results on stability and model calibration. Finally Section VIII concludes this article.

II. DESIGN CONSIDERATIONS OF MULTIARM MULTISTAGE ECCENTRIC TUBE ROBOTS

Considering a pair of arm channels, a schematic of the proposed continuum robot sheath is shown in Fig. 2. The two
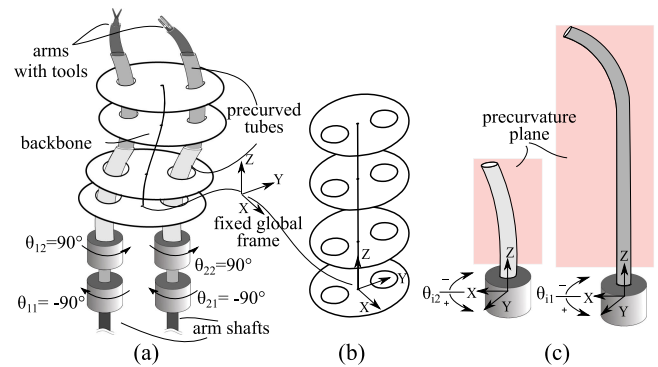

Fig. 2. Schematic of a steerable two-arm sheath. (a) Arm working channels are lined with precurved tubes that are rotated through the angles θ_{ij} to bend and straighten the sheath. (b) Central backbone is used to maintain disk spacing along the axis of the sheath. (c) Precurvature lies in the XZ plane and kinematic inputs consist of tube rotations measured with respect to initial configuration.

precurved tubes lining the arm channels can be rotated at the proximal end with respect to the sheath and with respect to each other. As depicted, the disks spaced along the length of the sheath are attached to a central backbone. These disks constrain the relative positions of the arm channel tubes. The role of the central backbone is solely to maintain the distance between the disks and so is assumed to be axially very stiff, but with arbitrary bending and torsional stiffness. This continuum mechanism is similar to the well-studied concentric tube balanced pair [27] except that the tubes are now offset from each other—forming what we term an eccentric tube robot. Depending on the selected bending and torsional stiffness of the central backbone, one can consider the overall structure to be comprised of three eccentrically arranged tubes.

We would like to select the precurvatures and relative stiffnesses of the two arm tubes so as to design a sheath that can deflect its tip in both the X and Y directions. It may also be necessary to rotate the arms about the Z-axis to correctly position the arms with respect to the surgical site. Consequently, we are also interested in how rotation of the working channel tubes may result in twisting of the sheath.

In order to avoid a hole in the middle of the workspace, we consider the case here in which the precurvature and stiffness of the two tubes are equal—matching the design of a concentric tube balanced pair. The kinematic configuration of Fig. 2(a) shows the case of a two-stage robot in which the precurvatures of the two tubes forming each section are aligned. We can anticipate that as both tubes of a specific section are simultaneously rotated, the tip of that section will roughly trace out a circle.

To straighten the sheath, the two tubes forming each section must be rotated such that their curvatures cancel each other. Three potential configurations for straightening a single-stage robot are shown in Fig. 3. In the configurations of Fig. 3(a) and (b), the tubes are coplanar. In Fig. 3(c), they are offset from each other, producing a moment with respect to the central axis. This configuration will likely result in a straight sheath that is twisted along its length.

For configurations consisting of rotations between the extreme cases of Figs. 2 and 3, we can anticipate that the sheath
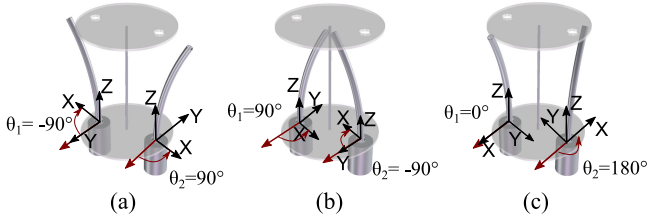
Fig. 3. Arm tube configurations to produce a straight sheath. Unconstrained tube shapes are depicted in order to make configurations clear. (a) Precurvatures are coplanar and facing away from each other. (b) Coplanar precurvatures are facing each other. (c) Precurvatures oppose each other, but are not coplanar.

will take on an intermediate value of curvature and of twist. To determine the specific relationship between arm tube angles $\{\theta_1, \theta_2\}$ and sheath shape along with the dependency on model parameters (e.g., arm eccentricity, disk spacing), we derive the kinematic model in the following section.

III. KINEMATIC MODELING

While a two-arm sheath design is described in the previous section, we consider here a sheath with arbitrary number of arms and tubes. To derive the model, which bears similarity to those previously proposed for push/pull tendon tubes [28], [29], the following assumptions are made.

1) Tubes and backbone are assumed to be flexible in bending and twisting, but axially rigid, and experience no cross-sectional shear deformation.
2) Disks are assumed to be rigid, perpendicular to the central backbone. They constrain centerline position of arm tubes, but not their orientation.
3) No external loads are applied.
4) Weights of disks, backbone and tubes are neglected.

The steerable sheath design proposed here and shown in Figs. 2 and 3 can be viewed as a structure composed of two constant-length concentric tube robots coupled by a set of disks to a straight compliant central backbone. The tubes of each working channel as well as the central backbone can be modeled individually using the Cosserat rod model. This is consistent with how concentric tube robot kinematics are derived [22], [25].

In a concentric tube robot, however, the common centerline arising from concentricity imposes two important constraints on the robot's cross section. First, when expressed in the same reference frame, the bending curvatures of the tubes are equal on a cross section. Second, the tubes do not slide relative to each other in the direction of arc length because they share a common neutral axis of bending.

These conditions do not hold for the proposed steerable sheath design. As can be seen in Fig. 2, while the working channels and central backbone are coupled, they have different radii of curvature on a cross section. This means that the working channel tubes must slide back and forth through the disks to provide the arc length commensurate with its arc length.

To take these factors into account, the bending curvatures of the working channels and the backbone have to be integrated independently and new variables are introduced to account for sliding of the working channel tubes through the disks.

TABLE I
NOMENCLATURE

i	Arm index with central backbone indexed as $i = 0$.
j	Tube index, numbered from inner to outer.
k	Disk index, numbered from the proximal end.
N	Total number of arms.
K	Total number of disks.
M	Total number of tubes in a section of an arm.
E, G	Young's and shear moduli.
I_i, J_i	Cross sectional area and polar moments of intertia of ith arm.
v	Poisson's ratio.
$\mathbf{K}_i, \mathbf{K}_{ij}$	Frame-invariant stiffness tensor of the ith arm (single stage) or the jth tube of the ith arm (multi-stage).
s_i	Arc length measured from the proximal end of ith arm.
s_{ik}	Arc length distance to the kth disk measured along the ith.
ℓ_i	Total arc length of ith arm.
ρ_j	Total arc length of the jth tube.
δ_{ik}	Difference in arc length to reach k^{th} disk along i^{th} arm versus along central backbone. See (11).
$\mathbf{r}_i, \|\mathbf{r}_i\|$	Position vector in local disk frame of hole in disk for i^{th} arm, the length is defined as the eccentricity.
$\mathbf{p}_i, \mathbf{p}_{ij}$	Position vector of ith arm (single stage) or the jth tube of the ith arm (multi-stage) in the global frame.
$\mathbf{v}_i$	Body frame three-component vector of linear strain rate per unit arc length of ith arm.
$\mathbf{u}_i, \mathbf{u}_{ij}$	Body frame three-component vector of curvature of ith arm (single stage) and the jth tube of the ith arm (multi-stage).
$\mathbf{R}_i, \mathbf{R}_{ij}$	Global frame rotation matrix of the ith arm (single stage) and the jth tube of the ith arm (multi-stage).
θ_i, θ_{ij}	Z-axis rotation angle with respective to global frame of ith arm (single stage) and the jth tube of the ith arm (multi-stage).
τ_{max}	Maximum Z-axis rotation angle with respective to global frame of the disk on the distal end.
α_{ij}	Relative Z-axis rotation between the jth tube and the innermost tube ($j = 1$) in local body frame on i^{th} arm.
β	Total angle swept out by precurved tube.
η	Relative stiffness of channel tube central backbone, κ_{1b}/κ_{0b}.
$\mu(s)$	Relative twist angle, $\theta_2(s) - \theta_1(s)$, between arm tubes.
$\mathbf{R}_{\alpha_{ij}}$	Rotation matrix for rotation of α_{ij} about Z-axis.
$\mathbf{m}_i, \mathbf{m}_{ij}$	Internal bending moment of the ith arm (single stage) and the jth tube of the ith arm (multi-stage) in local body frame.
$\mathbf{n}_i, \mathbf{n}_{ij}$	Shear force vector of the ith arm (single stage) and the jth tube of the ith arm (multi-stage) in local body frame.
$\mathbf{t}_i$	External distributed moment applied to the ith arm in local body frame.
$\mathbf{f}_i, \mathbf{f}_{ij}$	External distributed force applied to the ith arm (single stage) and the jth tube of the ith arm (multi-stage) in local body frame.
$\mathbf{g}_{ik}$	External point forces applied to the ith arm from k^{th} disk in the arm's body frame.
$\mathbf{h}_{ik}$	Point forces applied by the ith arm to the kth disk in the local disk frame.
$\mathbf{e}_z$	Unit Z-axis vector, i.e., $[0\ 0\ 1]^\top$.
$e_{p_{ik}}, e_1, w_1$	Relative position error of ith arm with respect to hole on k^{th}, sum of squared errors over all arms and disks, scalar weight for this term in optimization function, J.
$e_{f_{ik}}, e_2, w_2$	Error in force direction between i^{th} arm and the kth disk, sum of squared errors over all arms and disks, scalar weight for this term in optimization function, J.
$e_{\alpha_{ik}}, e_3, w_3$	Error in kinematic input variables (rotations at proximal ends of tubes), sum of squared errors over all tubes, scalar weight for this term in optimization function, J.
J, J_c	Optimization functions for kinematic solver and model calibration, respectively.
$\bullet^*$	Initial value of variable prior to deformation.
$\bullet\|_{x,y,z}$	Coordinate direction vector components.
$\hat{\bullet}$	Produces 3×3 skew-symmetric matrix form of a vector.
$\frac{d}{ds_i}, \dot{\bullet}, \ddot{\bullet}$	Derivatives with respect to arc length along the ith arm.

In this section, the kinematic model derivation proceeds as follows using the nomenclature defined in Table I. Equations (1)–(8) describe the Cosserat rod model, including external forces and moments, that must be integrated for the two working channels and for the central backbone. The boundary conditions arising from coupling between the working channels and backbone are described by (9)–(12). This includes concentrated forces applied to the working channels and forces plus moments
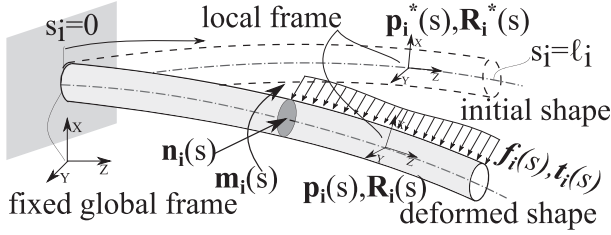
Fig. 4. Single precurved tube under an arbitrary external distributed force and moment load. The Bishop convention is used to define local frames along the rod as a function of arc length, i.e., the Z-axis is aligned with the tangent direction of the rod. For the rod without external load, the local frame is defined as if it slides from the proximal end to the distal end without Z-axis rotation.

applied to the backbone. In Section III-B, sliding between the working channels and disks is defined in (13), and is used to express the disk position constraints in (14) and the disk force equilibrium constraints in (15). Section III-C extends these equations to the case in which the working channels are each concentric tube robots.

As shown in Fig. 4, a fixed global frame can be defined at the proximal end while the solid and dashed lines show the initial and the deformed shapes of the rod, respectively. Each rod is parameterized by the curve length s_i with $s_i = 0$ at the cantilevered end, and $s_i = \ell_i$ at the distal end. The subscript $i \in [0, \ldots, N]$ denotes the index for the arms, and $i = 0$ stands for the central backbone. The variables $\mathbf{p}_i(s_i) \in \mathbb{R}^3$ and $\mathbf{R}_i(s_i) \in SO(3)$ are the position and orientation of the body local frame at s_i. A superscript $*$ is used to denote initial position and orientation. The derivative of position and orientation with respect to arc length s_i is defined as

$$\dot{\mathbf{p}}_i = \mathbf{R}_i \mathbf{v}_i, \quad \dot{\mathbf{R}}_i = \mathbf{R}_i \widehat{\mathbf{u}}_i. \tag{1}$$

Here, and in the following, the arc length variable s_i is omitted for brevity except where needed for clarity. The vectors $\mathbf{u}_i, \mathbf{v}_i \in \mathbb{R}^3$ are the angular and linear strain rates per unit arc length. The $\widehat{\cdot}$ operator defines a 3×3 skew-symmetric matrix from a 3-vector.

The rods are subject to arbitrary external distributed forces $\mathbf{f}_i$ and moments $\mathbf{t}_i$ defined with respect to the local body frame. The internal force $\mathbf{n}_i$ and moment $\mathbf{m}_i$ defined with respect to the local body frame at the cross section of position $\mathbf{p}_i$ are the resulting reaction force and moment from the external loads acting from s_i to ℓ_i. Expressed as a differential equation, the force and moment evolve with arc length according to

$$\begin{bmatrix} \dot{\mathbf{m}}_i \\ \dot{\mathbf{n}}_i \end{bmatrix} = \begin{bmatrix} \mathbf{t}_i \\ \mathbf{f}_i \end{bmatrix} - \begin{bmatrix} \widehat{\mathbf{u}}_i & \widehat{\mathbf{v}}_i \\ \mathbf{0} & \widehat{\mathbf{u}}_i \end{bmatrix} \begin{bmatrix} \mathbf{m}_i \\ \mathbf{n}_i \end{bmatrix}. \tag{2}$$

We can rewrite the moment equation in terms of curvature by introducing a constitutive equation. Assuming linear elastic behavior,

$$\mathbf{m}_i = \mathbf{K}_i(\mathbf{u}_i - \mathbf{u}_i^*), \quad \mathbf{K_i} = \begin{bmatrix} K_{ib} & 0 & 0 \\ 0 & K_{ib} & 0 \\ 0 & 0 & K_{it} \end{bmatrix} \tag{3}$$

in which $\mathbf{u}_i^* = [0\ u_{iy}^*\ 0]_{\mathsf{T}}$ stands for the predefined planar curvature of the ith tube, $\mathbf{K}_i$ is the stiffness matrix. Here, $K_{ib} = EI_i$ and $K_{it} = GJ_i$ are the bending and torsional stiffness of the tube

that are assumed constant along the tube length, respectively, E and G are the Young's and shear moduli, respectively, and $G = E/2(1 + \nu)$ where ν stands for the Poisson's ratio. I_i and J_i are the second moment of area and polar moment of the inertia of the cross section of the ith tube, respectively.

A. Modeling Single-Stage Robotic Sheaths

Given the assumption that disks constrain channel tube position, but not orientation, the interaction between disks and the channel tubes consists only of point forces. Between disks and the central backbone, the loading consists of point forces and point moments. Therefore, there are no distributed moments or forces applied ($\mathbf{t}_i = \mathbf{0}$ and $\mathbf{f}_i = \mathbf{0}$). The matrix equation (2) can be simplified as

$$\dot{\mathbf{m}}_i = -\widehat{\mathbf{u}}_i\, \mathbf{m}_i - \widehat{\mathbf{e}}_z\, \mathbf{n}_i \tag{4}$$

$$\dot{\mathbf{n}}_i = -\widehat{\mathbf{u}}_i\, \mathbf{n}_i$$

$$= \begin{bmatrix} -\mathbf{u}_i|_y\, \mathbf{n}_i|_z + \mathbf{u}_i|_z\, \mathbf{n}_i|_y \\ \mathbf{u}_i|_x\, \mathbf{n}_i|_z - \mathbf{u}_i|_z\, \mathbf{n}_i|_x \\ -\mathbf{u}_i|_x\, \mathbf{n}_i|_y + \mathbf{u}_i|_y\, \mathbf{n}_i|_x \end{bmatrix} \tag{5}$$

where $\mathbf{v}_i = \mathbf{e}_z = [0, 0, 1]^{\mathsf{T}}$ since we assume that shear strain and axial strain are negligible.

Assuming that the precurvature $\mathbf{u}_i^*$ is piece-wise constant, differentiating (3) in segments of constant curvature and substituting it into (4) yields a differential equation in curvature given by

$$\dot{\mathbf{u}}_i = -\mathbf{K}_i^{-1} \left[\widehat{\mathbf{u}}_i \mathbf{K}_i (\mathbf{u}_i - \mathbf{u}_i^*) + \widehat{\mathbf{e}}_z \mathbf{n}_i \right]$$

$$= \begin{bmatrix} -\frac{K_{it}}{K_{ib}} \mathbf{u}_i|_y (\mathbf{u}_i|_z - \mathbf{u}_i^*|_z) + \mathbf{u}_i|_z (\mathbf{u}_i|_y - \mathbf{u}_i^*|_y) + \frac{\mathbf{n}_i|_y}{K_{ib}} \\ \frac{K_{it}}{K_{ib}} \mathbf{u}_i|_x (\mathbf{u}_i|_z - \mathbf{u}_i^*|_z) - \mathbf{u}_i|_z (\mathbf{u}_i|_x - \mathbf{u}_i^*|_x) - \frac{\mathbf{n}_i|_x}{K_{ib}} \\ \frac{K_{ib}}{K_{it}} (\mathbf{u}_i|_x \mathbf{u}_i^*|_y - \mathbf{u}_i|_y \mathbf{u}_i^*|_x) \end{bmatrix}. \tag{6}$$

Equations (5) and (6) comprise the set of equations that must be solved between each pair of disks to compute curvature along each section of the tubes and the backbone.

For the single-stage eccentric tube sheath, the disks divide the whole length into sections, which are defined as the region between two consecutive disks. While the central backbone ends at the distal disk, the distal section of the channel tubes is defined as extending from the distal disk to the ends of the tubes. Therefore, the boundary conditions of the channel tubes at the last section for solving curvature and internal force are as follows:

$$\mathbf{u}_i(\ell_i) = \mathbf{u}_i^*, \quad \mathbf{n}_i(\ell_i) = \mathbf{0}. \tag{7}$$

The curvature is continuous along the whole arc length; however, the tubes interact with the disks at discrete points along their length. The interaction forces between the tubes and disks are point forces, as shown in Fig. 5(a). Under the frictionless assumption, the point forces $\mathbf{g}_{ik}$ exerted by the kth disk ($k \in [1, \ldots, K]$) on the ith channel should be perpendicular to the outermost interacting tube, resulting in $\mathbf{g}_{ik} = [\mathbf{g}_{ik}|_x, \mathbf{g}_{ik}|_y, 0]^{\mathsf{T}}$. Consequently, the boundary conditions of the channel tubes in
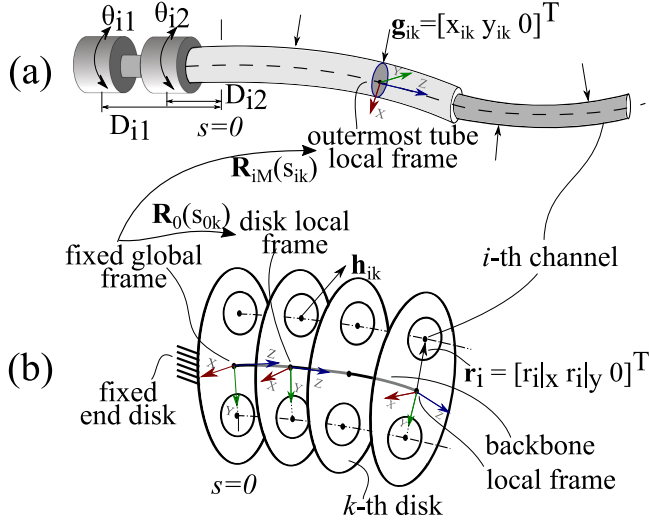
Fig. 5. Interaction between the ith working channel and the kth disk. (a) ith channel is subject to external point forces $\mathbf{g}_{ik}$ from the kth disk. (b) Backbone together with the disks can be regarded as a single cantilevered rod subjected to external point forces $\mathbf{h}_{ik}$.

the middle are as follows:

$$\mathbf{u}_i(s_i^-) = \mathbf{u}_i(s_i^+) \quad \mathbf{n}_i(s_{ik}^-) = \mathbf{n}_i(s_{ik}^+) + \mathbf{g}_{ik} \qquad (8)$$

where s_{ik}^- and s_{ik}^+ denote the arc length of the ith tube before $(-)$ and after $(+)$ the kth disk.

The boundary conditions of the backbone $(i = 0)$ express the discontinuities in internal force and moment at each disk. The reaction forces from channel tubes, $\mathbf{h}_{ik}$, acting on the disks will generate both forces and moments on the central backbone. It is noted that the moments will be generated due to the eccentricity $\mathbf{r}_i = [\mathbf{r}_i|_x, \mathbf{r}_i|_y, 0]^\intercal$. Referring to Fig. 5(b), the boundary conditions of the backbone at the end disk are given by

$$\mathbf{m}_0(\ell_0) = \mathbf{0}, \quad \mathbf{n}_0(\ell_0) = \sum_{i=1}^{N} \mathbf{h}_{iK} \qquad (9)$$

and in the middle are given by

$$\mathbf{m}_0(s_{0k}^-) = \mathbf{m}_0(s_{0k}^+) + \sum_{i=1}^{N} (\mathbf{r}_i \times \mathbf{h}_{ik})$$

$$\mathbf{n}_0(s_{0k}^-) = \mathbf{n}_0(s_{0k}^+) + \sum_{i=1}^{N} \mathbf{h}_{ik}. \qquad (10)$$

B. Compatibility Conditions Imposed by Disks

Integrating backward in arc length from ℓ_i to 0 yields the curvature along the ith arm channel and backbone. As will be shown for multistage designs, this will also yield the torsional twisting of all tubes comprising an arm channel. Curvature can be simultaneously integrated along the robot's length to yield the tip position and orientation relative to the global frame, which is fixed with respect to the proximal disk, as shown in Fig. 5. At the proximal disk $(k = 1)$, each channel tube is constrained to be tangent to the central backbone along the Z-axis.

Because the arm channels can possess different bending curvatures from each other and from the central backbone, the arc lengths at which they pass through each disk varies with configuration. To account for this variation, we introduce a variable δ_{ik} to model the sliding of the channel tubes with respect to the disks

$$s_{ik} = s_{0k} + \delta_{ik} \qquad (11)$$

where s_{ik} and s_{0k} are the arc lengths of the ith working channel and the backbone at the kth disk, respectively. The disks constrain the positions of the arms with respect to central backbone following

$$\mathbf{p}_i(s_{ik}) = \mathbf{R}_0(s_{0k})\mathbf{r}_i + \mathbf{p}_0(s_{0k}) \qquad (12)$$

where $\mathbf{R}_0$ denotes the backbone orientation.

When expressed in the same frame, the forces $\mathbf{g}_{ik}$ and $\mathbf{h}_{ik}$ are equal in magnitude and opposite in direction. In the following, $\mathbf{R}_i(s_{ik})$ and $\mathbf{R}_0(s_{0k})$ are used to transform $\mathbf{g}_{ik}$ and $\mathbf{h}_{ik}$, respectively, to a common global frame

$$\mathbf{R}_i(s_{ik})\,\mathbf{g}_{ik} + \mathbf{R}_0(s_{0k})\mathbf{h}_{ik} = \mathbf{0}. \qquad (13)$$

C. Modeling Multistage Robotic Sheaths

For a multistage sheath, the working channels are each concentric tubes robots subjected to external loads imposed by the backbone through the disks. In our previous work, we have presented kinematic models for concentric tube robots subject to external loads [30], [31]. The model of [31] is used here to simplify the derivation.

We now consider the case of M concatenated steerable stages. Each stage is controlled by its precurved outermost tube. The tubes for controlling each distal section are nested within and are selected to be both straight (no precurvature) and compliant in comparison with the outer tubes. Their compliance ensures that they do not significantly reduce the precurvature of the outer tube. Each tube is designated by its arm index $i \in [1, \dots, N]$ and by its tube number $j \in [1, \dots, M]$. Here, $j = 1$ denotes the innermost tube and $j = M$ denotes the outermost one. Note that the number of tubes is M in the proximal stage and 1 in the distal stage.

Since the tubes for each arm are concentric, they share the same center line as $\mathbf{p}_{i1} = \cdots \mathbf{p}_{ij} \cdots = \mathbf{p}_{iM}$, where $\mathbf{p}_{ij}$ is the position of the jth tube of the ith arm channel. Their body coordinate frames differ only by a rotation about the tangent Z-axis. If we define the relative rotation of each tube with respect to the innermost tube by the angle $\alpha_{ij} = \theta_{ij} - \theta_{i1}$, then we can write

$$\mathbf{u}_{ij} = \mathbf{R}_{\alpha_{ij}}^\intercal \mathbf{u}_{i1} + \dot{\alpha}_{ij}\mathbf{e}_z = \begin{bmatrix} \mathbf{u}_{i1}|_x \cos(\alpha_{ij}) + \mathbf{u}_{i1}|_y \sin(\alpha_{ij}) \\ \mathbf{u}_{i1}|_y \cos(\alpha_{ij}) - \mathbf{u}_{i1}|_x \sin(\alpha_{ij}) \\ \dot{\alpha}_{ij} + \mathbf{u}_{i1}|_z \end{bmatrix}$$

$$(14)$$

$$\dot{\alpha}_{ij} = \mathbf{u}_{ij}|_z - \mathbf{u}_{i1}|_z \qquad (15)$$

where $\mathbf{u}_{ij}$ is the curvature of the jth tube of the ith arm channel.

Writing (2) for each tube in an arm, these equations become

$$\dot{\mathbf{m}}_{ij} = -\widehat{\mathbf{u}}_{ij}\,\mathbf{m}_{ij} - \widehat{\mathbf{e}}_z\,\mathbf{n}_{ij} \tag{16}$$

$$\dot{\mathbf{n}}_{ij} = \mathbf{f}_{ij} - \widehat{\mathbf{u}}_{ij}\,\mathbf{n}_{ij}\,. \tag{17}$$

1) Differential Equations for CTR With External Concentrated Forces: Differential equation for torsional twisting of arm tubes, we extract the expression for the z component as

$$\dot{\mathbf{u}}_{ij}|_z = \frac{K_{ij_b}}{K_{ij_t}}\left(\mathbf{u}_{ij}|_x \mathbf{u}_{ij}^*|_y - \mathbf{u}_{ij}|_y \mathbf{u}_{ij}^*|_x\right)\,. \tag{18}$$

In the case that the precurvatures of all tubes but the outermost are zero and the precurvature of the outer tube is in the Y coordinate direction, this simplifies to

$$\dot{\mathbf{u}}_{ij}|_z = \begin{cases} \frac{K_{ij_b}}{K_{ij_t}}\left(\mathbf{u}_{i1}|_x \cos(\alpha_{ij}) + \mathbf{u}_{i1}|_y \sin(\alpha_{ij})\right)\mathbf{u}_{ij}^*|_y & j = M \\ 0 & j \neq M \end{cases}\,. \tag{19}$$

Defining $\mathbf{K}_i = \sum_{j=1}^{M} \mathbf{K}_{ij}$ and $\mathbf{n}_i = \sum_{j=1}^{M} \mathbf{R}_{\alpha_{ij}}\mathbf{n}_{ij}$, the differential equation for the bending curvature of innermost tube $(j{=}1)$ can be derived in the same manner as in [30], as follows:

$$\dot{\mathbf{u}}_{i1}|_{xy} = \mathbf{K}_i^{-1}\left(\sum_{j=1}^{M}\dot{\alpha}_{ij}\mathbf{K}_{ij}\right)\widehat{\mathbf{e}}_z\,\mathbf{u}_{i1}\Bigg|_{xy}$$

$$- \mathbf{K}_i^{-1}\Bigg(\left(\sum_{j=1}^{M}\ddot{\alpha}_{ij}\mathbf{R}_{\alpha_{ij}}\mathbf{K}_{ij}\right)\mathbf{e}_z + \widehat{\mathbf{u}}_{i1}\mathbf{K}_i\mathbf{u}_{i1}$$

$$+ \left(\sum_{j=1}^{M}\dot{\alpha}_{ij}\mathbf{K}_{ij}\right)\widehat{\mathbf{e}}_z\,\mathbf{u}_{i1} + \sum_{j=1}^{M}\dot{\alpha}_{ij}K_{ij_t}\begin{bmatrix}\mathbf{u}_{i1}|_y \\ -\mathbf{u}_{i1}|_x \\ 0\end{bmatrix}$$

$$+ K_{iMb}\,\mathbf{u}_{iM}^*|_y\left(\widehat{\mathbf{u}}_{i1}\begin{bmatrix}\sin(\alpha_{1M}) \\ -\cos(\alpha_{1M}) \\ 0\end{bmatrix} + \dot{\alpha}_{iM}\begin{bmatrix}\cos(\alpha_{1M}) \\ \sin(\alpha_{1M}) \\ 0\end{bmatrix}\right)$$

$$+ \widehat{\mathbf{e}}_z\,\mathbf{n}_i\Bigg)\Bigg|_{xy}\,. \tag{20}$$

Here, we have used the fact that only tube M has a nonzero precurvature.

Equations (15), (18), and (20) provide the differential equations for curvature, but they require the value of total shear stress on the channel arm, $\mathbf{n}_i$. Following the method as in [30], $\mathbf{n}_i$ can be obtained using the special Cosserat shear force equation (17) as follows:

$$\dot{\mathbf{n}}_i = -\widehat{\mathbf{u}}_{i1}\,\mathbf{n}_i\,. \tag{21}$$

This is equivalent to (17), but for the net shear force on the collection of tubes comprising the ith arm.

2) Multistage Boundary Conditions: Equations (15), (18), (20), and (21) comprise the set of differential equations to be solved for α_{ij}, $\mathbf{u}_{ij}|_z$, $\mathbf{u}_{i1}|_{xy}$, and $\mathbf{n}_i$, respectively, to obtain the shape of the M tubes comprising an arm channel. Since the backbone is a single tube, its shape can continue to be solved for using (5) and (6).

For a single-stage system with N arms plus the central backbone, one must solve for a total of $6(N + 1)$ curvatures and shear force state variables. In the multistage case, for each arm, there are $M - 1$ variables for α_{ij}, two variables for $\mathbf{u}_{i1}|_{xy}$, M variables for $\mathbf{u}_{ij}|_z$, and three variables for $\mathbf{n}_i$, totaling $2M + 4$ integration variables.

Similar to the single-section case, the interaction between disks and tubes consists only of point forces. Therefore, the boundary conditions for the backbone remain the same as in (9) and (10).

The boundary conditions of the channel tubes at the distal and proximal ends are as follows:

$$\mathbf{u}_{ij}(\ell_i) = \mathbf{u}_{ij}^*\,, \quad \mathbf{n}_i(\ell_i) = \mathbf{0}$$

$$\alpha_{ij}(0) = (\theta_{ij}(0) + D_{ij}\mathbf{u}_{ij}|_z(0)) - (\theta_{i1}(0) + D_{i1}\mathbf{u}_{i1}|_z(0)) \tag{22}$$

where D_{ij} denotes the transmission length of the jth tube of the ith arm. The boundary conditions of the channel tubes in the middle section of the same stage are as follows:

$$\mathbf{u}_{ij}(s_i^-) = \mathbf{u}_{ij}(s_i^+) \quad \alpha_{ij}(s_i^-) = \alpha_{ij}(s_i^+)$$

$$\mathbf{n}_i(s_{ik}^-) = \mathbf{n}_i(s_{ik}^+) + \mathbf{R}_{\alpha_{ij}}\mathbf{g}_{ik}\,. \tag{23}$$

As shown in Fig. 5(a), the tube ending effect should be also considered in terms of boundary conditions of the internal moment and force. Let the arc length at the end of the jth tube be $s_i = \rho_j$ on the ith arm. Because there is no external force input, the internal force will be continuous as

$$\mathbf{n}_i(\rho_j^-) = \mathbf{n}_i(\rho_j^+)\,. \tag{24}$$

Because the concentric tubes are allowed to freely twist within each other, when $j \in [1, \ldots, M-1]$, the torsional curvature and the relative twist angle will have the continuity condition as

$$\mathbf{u}_{ij}(\rho_j^-)\,|_z = \mathbf{u}_{ij}(\rho_j^+)\,|_z \quad \alpha_{ij}(\rho_j^-) = \alpha_{ij}(\rho_j^+)\,. \tag{25}$$

For the Mth tube, the torsional curvature is given by

$$\mathbf{u}_{iM}(\rho_j^-)\,|_z = \mathbf{u}_{iM}^*|_z = 0\,. \tag{26}$$

The boundary conditions for the bending curvature can be found using the moment equilibrium and the constitutive equation (3). The internal bending moments before $(-)$ and after $(+)$ the end of the outermost tube can be expressed in the innermost tube frame as

$$\mathbf{m}_i(\rho_j^+)\Bigg|_{xy} = \mathbf{R}_{\alpha_{i(M-1)}}(\rho_j^+)\,\mathbf{K}_{i(M-1)}\Bigg(\mathbf{u}_{i(M-1)}(\rho_j^+)$$

$$- \mathbf{u}_{i(M-1)}^*\Bigg)$$

$$+ \left(\sum_{j=1}^{M-2}\mathbf{R}_{\alpha_{ij}}(\rho_j^+)\,\mathbf{K}_{ij}\,\mathbf{u}_{ij}(\rho_j^+)\right)\Bigg|_{xy}$$

$$\mathbf{m}_i(\rho_j^-)\Bigg|_{xy} = \mathbf{R}_{\alpha_{iM}}(\rho_j^-)\,\mathbf{K}_{iM}\left(\mathbf{u}_{iM}(\rho_j^-) - \mathbf{u}_{iM}^*\right)$$

$$+ \left(\sum_{j=1}^{M-1} \mathbf{R}_{\alpha_{ij}}(\rho_j^+) \, \mathbf{K}_{ij} \, \mathbf{u}_{ij}(\rho_j^+) \right) \Bigg|_{xy}. \quad (27)$$

Since there is no external bending moment, we have $\mathbf{m}_i(\rho_j^-)|_{xy} = \mathbf{m}_i(\rho_j^+)|_{xy}$. After substituting (14) and some manipulations, we have the following boundary condition for the bending curvature:

$$\mathbf{u}_{i1}(\rho_j^-) \Bigg|_{xy} = \mathbf{K}_i(\rho_j^-)^{-1} \Bigg(\mathbf{K}_i(\rho_j^+)\mathbf{u}_{i1}(\rho_j^+) + \mathbf{R}_{\alpha_{iM}}(\rho_j^-)\mathbf{K}_{1M}\mathbf{u}_{iM}^*$$
$$- \mathbf{R}_{\alpha_{i(M-1)}}(\rho_j^+)\mathbf{K}_{1(M-1)} \, \mathbf{u}_{i(M-1)}^* \Bigg) \Bigg|_{xy}. \quad (28)$$

3) Multistage Disk Compatibility Equations: Similar to the single-stage design, the arm tubes can slide in the arc length direction through the holes in the disks. The position compatibility constraint below allows for this difference in arc length, given by (11)

$$\mathbf{p}_{i1}(s_{ik}) = \mathbf{R}_0(s_{0k})\mathbf{r}_i + \mathbf{p}_0(s_{0k}). \quad (29)$$

Similarly, the interaction forces $\mathbf{g}_{ik}$ acting on the outermost tube of the ith arm are equal and opposite to the forces applied to the disks when both are expressed in a common global frame

$$\mathbf{R}_{iM}(s_{ik}) \, \mathbf{g}_{ik} + \mathbf{R}_0(s_{0k})\mathbf{h}_{ik} = \mathbf{0}. \quad (30)$$

D. Solution Approach

A shooting method is used to compute numerical solutions to the kinematic model. Similar to concentric tube robot equations, channel tube rotations at the proximal end are the kinematic input variables. The unknown boundary conditions for concentric tubes also carry over and apply to both the working channel tubes and the central backbone, namely, twist angles at the distal ends and the orientations of external loads applied by the disks to the channel tubes. Additional unknown boundary conditions for the eccentric sheath include the channel tube arc-length displacements relative to the disks as described by (13) and the magnitudes of the reaction forces acting between the channel tubes and the disks. The overall approach is to assume values for all of the unknown boundary conditions and, using those values, to integrate the differential equations for the channel tubes and central backbone simultaneously, but independently.

An optimization method is used to iteratively reduce an error function based on these unknown boundary conditions. The error function given below has three components. The first e_1 computes the relative position errors while the second e_2 computes the angles between the forces applied to the channel tubes and the forces applied to the disks. The third component e_3 computes the difference between the specified and computed twist angles at the proximal ends of the channel tubes

$$e_1 = \sum_{i=1}^{N} \sum_{k=2}^{K} e_{pik}^2, \quad e_{pik} = \|\mathbf{p}_{i1} - \mathbf{R}_0\mathbf{r}_i - \mathbf{p}_0\| \quad (31)$$

$$e_2 = \sum_{i=1}^{N} \sum_{k=2}^{K} e_{fik}^2, \quad e_{fik} = \frac{180}{\pi} \arccos \left(\frac{-\mathbf{h}_{ik}^\mathsf{T} \mathbf{R}_0^\mathsf{T} \, \mathbf{R}_{iM}\mathbf{g}_{ik}}{\mathbf{g}_{ik}|_x^2 + \mathbf{g}_{ik}|_y^2} \right) \quad (32)$$

$$e_3 = \sum_{i=1}^{N} \sum_{j=2}^{M} e_{\alpha ij}^2, \quad e_{\alpha ij} = \frac{180}{\pi} \left(\alpha_{ij}(0) - \widetilde{\alpha}_{ij}(0) \right) \quad (33)$$

where $\widetilde{\alpha}_{ij}$ denotes the computed relative rotation angle of the jth tube at the ith arm that can be integrated backward from either the initial guess or the preceding iteration of the relative rotation angle $\alpha_{ij}(\rho_j)$ at the end of the jth tube; α_{ij} can be found by (22).

The optimization function can then be defined as follows:

$$J = w_1 \, e_1 + w_2 \, e_2 + w_3 \, e_3 \quad (34)$$

where $w_{1,2,3} > 0$ are the scalar weights.

The optimization problem is to minimize this function with respect to the following variables.

1) Force magnitude and direction from each arm on each disk, $\mathbf{h}_{ik}$, plus the force direction from each disk on each arm, $\mathbf{g}_{ik}$. (Note that, assuming frictionless tubes, a single parameter describes the force direction on each arm, and its magnitude can be selected to match $\mathbf{h}_{ik}$.)
2) Arc length displacements δ_{ik} representing the sliding of the channel tubes with respect to the disks. [See (11).]
3) Twist angles at the distal ends of the channel tubes, $\alpha_{ij}(\rho_j)$.

The optimization is initialized using guesses for these variables. Since the arc length displacements δ_{ik} are anticipated to be small, they can be initialized to zero. While the force directions and magnitudes are difficult to guess for an arbitrary initial configuration, continuity can be used to initialize configurations in the neighborhood of a known solution. Using this approach, it is possible to start in a configuration in which force terms are easier to predict, such as when all arms have their precurved tubes aligned and oriented symmetrically with respect to the central backbone such that no twisting moments are applied to the tubes.

Using MATLAB's *fmincon* and *sqp* algorithms, the kinematic equations are solved iteratively until a specified convergence criterion is met. Constraints on sliding variables are specified as $|\delta_{ik}| < \ell_0/K$ to eliminate collisions on disks.

The kinematic function evaluation consists of independently integrating from tip to base the differential equations for the collections of channel tubes as well as the central backbone. The result of this integration is the shape of each arm and that of the central backbone based on the assumed values of $\mathbf{h}_{ik}$, δ_{ik}, and ω_{ij}. The optimization routine uses the cost function (34) to adjust the parameter values.

To determine convergence, we are interested in maximum errors rather than mean square errors. Therefore, we employ the following convergence criterion in which γ_p, γ_f, and γ_α are the maximum allowed errors, respectively, in the relative position of an arm with respect to a disk, angular mismatch in the force direction of an arm on a disk, and twist angles at the distal end

	Arm tube	Backbone
Nominal bending stiffness (N·m^2)	1.40×10^{-3}	1.40×10^{-3}
Poisson's ratio	0.33	0.33
Precurvature angle (°)	80 / 100	0
Radius of precurvature (mm)	85.944 / 68.755	∞
Total arc length (mm)	120	100

of each tube:

$$\max_{i,k} e_{pik} \leq \gamma_p \bigwedge \max_{i,k} e_{fik} \leq \gamma_f \bigwedge \max_{i,j} e_{\alpha ij} \leq \gamma_\alpha . \tag{35}$$

For the robot designs described in this article, the values of the various weights were initially hand selected, such as $w_{1,2,3} = [1, 1, 1]^\mathsf{T}$, and subsequently tuned manually.

In the solution approach described above, the differential equations for the channel tubes and central backbone are integrated using forces described in the body frames. These forces are converted to a common global frame for evaluation of the error function (32). This enables the three differential equations to be integrated in parallel during each iteration. In comparison, our prior solution approach in [26] performed integration in two steps. The arm channel differential equations were first integrated using body frame forces to solve for the channel tube shapes. The shapes were then used to convert the body frame forces to global frame forces applied to the central backbone. The differential equation for the central backbone was then integrated using these global frame forces. This approach ensured that equal and opposite forces were applied to the channel tubes and central backbone at each iteration, but the method would fail to converge if the initial guess for the backbone shape was not close to the actual solution. The solution approach described above was found to be more robust with respect to initial guesses.

IV. EFFECT OF DISK NUMBER

The disks constrain the deformation of the channel tubes to follow that of the central backbone. Using too few disks results in channel tube shapes that bulge away from the central backbone. Since each disk introduces $5N$ variables, however, it is desirable to use the minimum number of disks needed to constrain the channel tubes. To investigate the effect of disk number on channel tube shape, we defined a compactness metric C, which compares the centerline positions of the channel tubes computed based on a finite number of disks with the arm hole positions for an infinite number of virtual disks

$$C(\boldsymbol{\theta}) = \max_{i \in [1,N]} \max_{s_0 \in [0,\ell_0]} \|\mathbf{p}_{i1} - \mathbf{R}_0 \mathbf{r}_i - \mathbf{p}_0\| . \tag{36}$$

For a vector of kinematic input angles $\boldsymbol{\theta}$, it is defined as the maximum distance from all channel tubes to the corresponding holes on the corresponding virtual disk.

Most of the examples in this article involve a single-stage two-arm system. Using the parameters listed in Table II, we computed the compactness metric for disk numbers $k = \{2, 3, \ldots, 11\}$ using 16 uniformly sampled arm angle configurations to produce the results shown in Fig. 6.
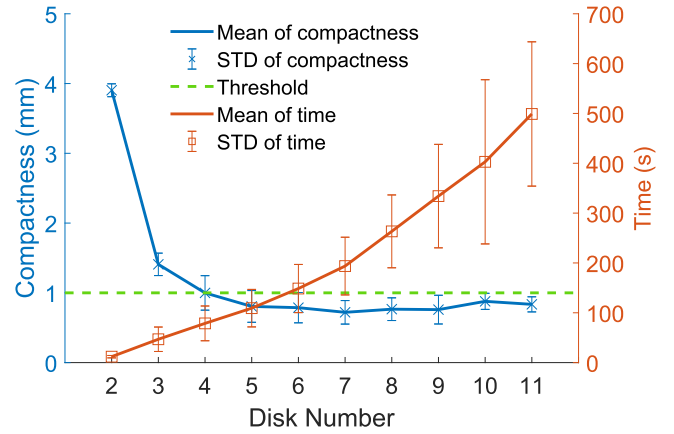

Fig. 6. Compactness metric and computation time versus disk number.

The mean and the standard deviation of the compactness metric converge for disk numbers of 4 or greater. As a conservative choice, six disks are used in the examples in the rest of the article.

V. WORKSPACE CHARACTERIZATION

Given that the precurved tubes for each stage are selected to be of the same stiffness and precurvature, each sheath section sweeps out a solid angle that includes the straight configurations shown in Fig. 3. The workspace boundary is achieved for equal values of channel tube arm angles, e.g., $\theta_1 = \theta_2$ at which the arm precurvatures are aligned. Four such configurations are shown in Fig. 7(a). Notice how on the workspace boundary, the arm channels do not experience any roll or twisting with respect to the sheath. Another interesting thing to note is that the maximum curvature is constant around the boundary.

Consider that the configurations B and D occur when the precurved tubes lie on the neutral axis of bending. In this case, it can be anticipated that the resultant curvature can be calculated by considering the precurved tubes and backbone as parallel springs of equal curvature. The fact that configurations A and C have the same backbone curvature as those of B and D is perhaps a little surprising since neither precurved tubes lies on the neutral axis for these configurations. Thus, the two tubes and the backbone all have different radii of curvature. Nevertheless, the neutral axis curvature remains constant as the sheath traces out its workspace boundary.

The workspace of multistage sheaths [Fig. 7(b)] is formed by concatenating the single-stage workspaces. Note, though, that the tubes of distal stages reduce the curvature of proximal stages.

A. Workspace Interior

To reach sheath curvatures between zero and the maximum value, the relative angle between the two tube angles can be varied between 0 and π. The sheath will trace out a circle of constant curvature for any fixed relative angle in this range, as shown by the red circle in Fig. 7(a). When keeping one tube angle constant and rotating the other through 2π, the sheath will trace out a smaller circle as depicted by the green circle. In the
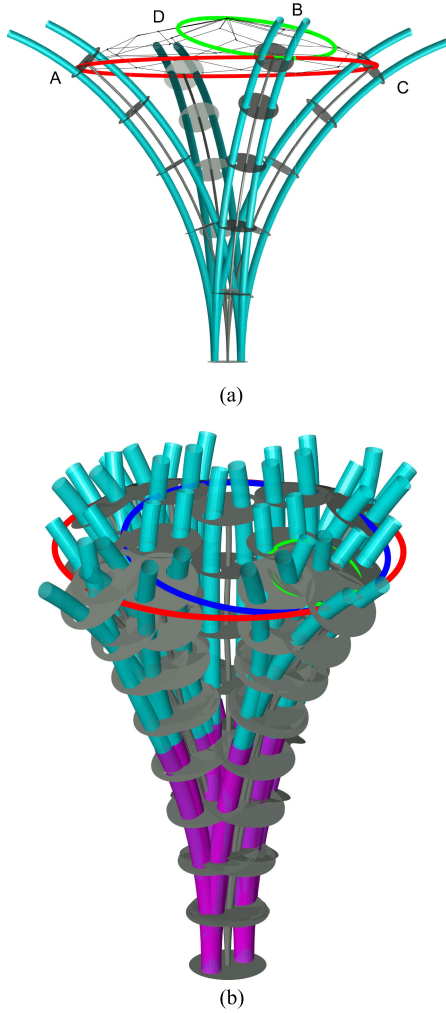
(a)

(b)

Fig. 7. Workspace of single- and two-stage ETRs. (a) Two-arm single-stage sheath with parameters listed in Table II. Depicted configurations lie on workspace boundary. Red circle (radius=43.5 mm) traces the tip of the central backbone on the workspace boundary while green circle (radius=23.0 mm) traces the motion boundary while keeping one tube angle constant and rotating the other through 2π. (b) Two-arm two-stage sheath with parameters listed in Table VI. Red circle (radius=22.5 mm) traces the tip of the central backbone on the workspace boundary, while blue (radius=17.1 mm) and green (radius=6.1 mm) circles trace the motion boundary when keeping the distal and proximal section pairs of tubes fixed, respectively, while rotating the other through 2π. Best viewed in the color.

interior of the workspace, the sheath typically experiences some twist at the tip as described in more detail below.

B. Sheath Twisting

The sheath assumes a straight configuration for tube angles such as those of Fig. 3. In the two configurations of Fig. 3(a) and (b), the curvature of the arm tubes lie in the same plane as the central backbone and so the sheath does not twist. For the configuration of Fig. 3(c), however, the precurvature of the arm tubes creates a twisting moment on the central backbone. This is depicted in Fig. 8, which shows the twisting of the sheath for two values of eccentricity with the twist angle given by $\theta_0(\ell_0) = \tau_{\max}$. As the arm tubes rotate from this configuration while satisfying $\theta_1 = \theta_2 + \pi$, the twist angle of the sheath varies
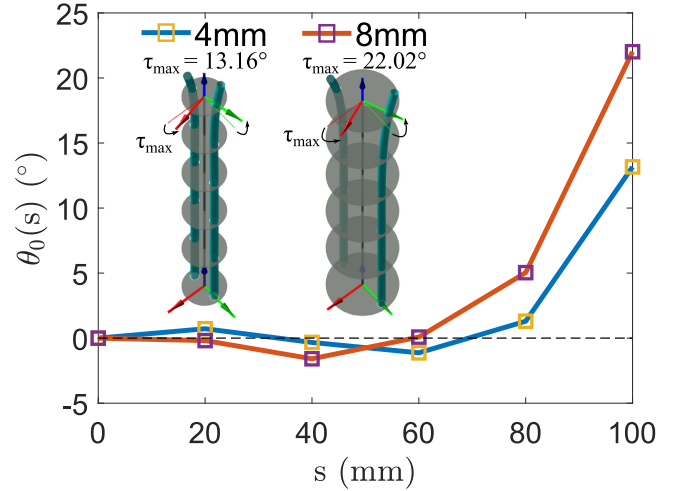

Fig. 8. Twisting of single-stage sheath with different offsets in straight configuration. The square mark denotes the twist angle at each disk. Best viewed in color.

over an angle range of $|\theta_0(\ell_0)| \leq \tau_{\max}$. As shown in Fig. 8, $\tau_{\max} = \pm 13.16°$ for a 4-mm offset. For an 8-mm offset, $\tau_{\max}$ increases to $\pm 22.02°$. This increase can be anticipated since the offset determines the torsional moment that the arms produce on the central backbone. Notice from the plots that the twisting is minimal and reverses direction between the proximal disks with the majority of twist occurring between the distal two pairs of disks.

As described in the following section, the configuration of Fig. 3(b), in which the arm tube precurvatures are facing each other, can produce sheath twisting when the robot is unstable. In this situation, there are two solutions corresponding to the two twisting directions, as will be explained for Fig. 10(d).

VI. ELASTIC STABILITY

Elastic instability of eccentric tube sheaths can occur in a similar fashion to concentric tube robots, i.e., when the relative rotation angle between the arm tubes is $180°$ at their base. Fig. 3 depicts three such configurations. Torsional twisting of the channel tubes can result in a sudden snapping of tubes with respect to the central backbone to reach a configuration of lower elastic energy. While an analytic derivation of stability is not attempted here, the dependence of stability on design parameters is qualitatively explored.

Considering a robotic sheath comprised of two precured channel tubes, stability can be depicted graphically by plotting the relative rotation angle of the two tubes at their tip with respect to their base. This technique has been used for concentric tubes, as shown in [22] and [32]. Defining the relative twist angle as

$$\mu(s) = \theta_2(s) - \theta_1(s) \qquad (37)$$

simulations have been carried out to find relative twist angles at the distal end $\mu(\ell)$ under different relative twist angles at the proximal end $\mu(0)$. Note that since the channel tubes can be rotated independently, different plots can be generated for specific values of $\theta_1(0)$. Using the design parameters listed in
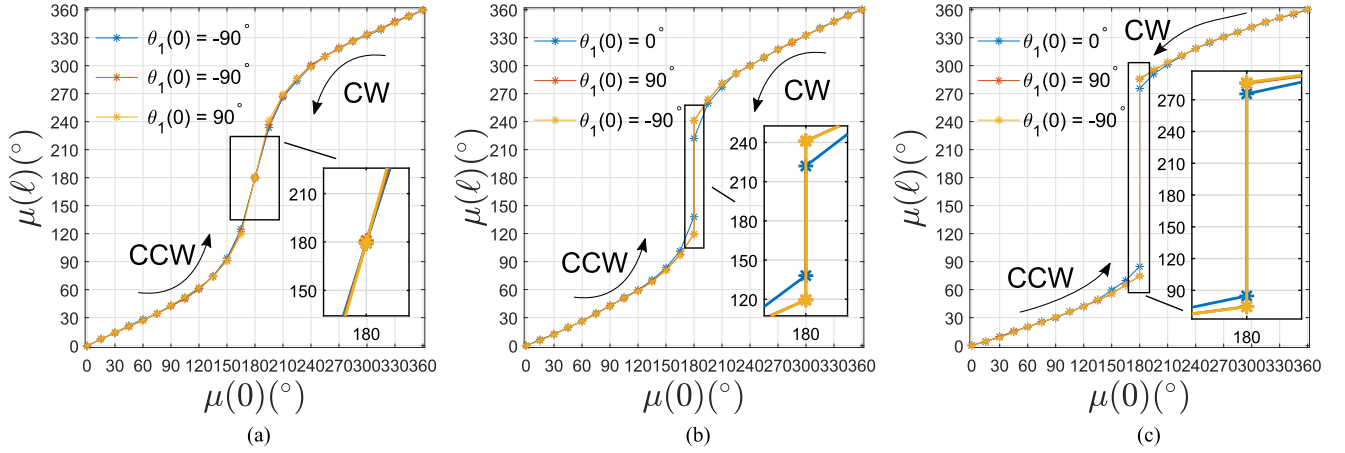
Fig. 9.   Relative rotation angle of channel tubes at their tip versus their base. (a) Stable design with channel tubes precurved through 100°. (b) Unstable design with channel tubes precurved through 100° and a 17-mm transmission length. (c) Unstable design with channel tubes precurved through 120° and a 17-mm transmission length. Best viewed in color.
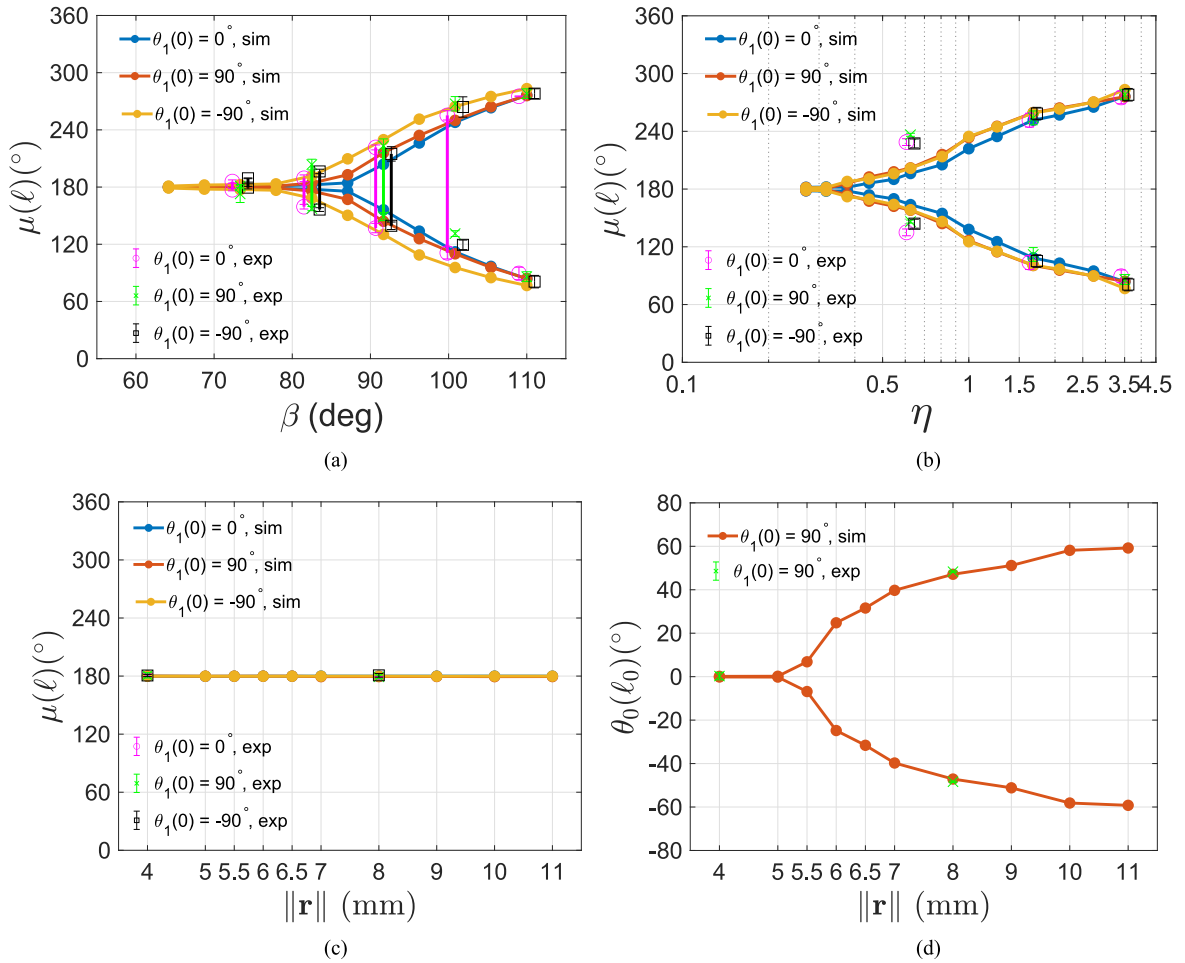

Fig. 10.   Stability as a function of precurvature, relative bending stiffness, and eccentricity. (a) Effect of precurvature angle β on the relative arm tip twist angle $\mu(\ell)$ for stiffness ratio $\eta = 3.51$ (calibrated), and eccentricity, $\|\mathbf{r}\| = 4$ mm and 12 mm transmission lengths. Solid vertical lines connecting upper and lower branches denote a continuous family of solutions for the experimental system. Lines are slightly offset in angle for visualization. (b) Effect of relative bending stiffness η on the relative arm tip twist angle $\mu(\ell)$ for $\beta = 110°$, and eccentricity $\|\mathbf{r}\| = 4$ mm and 12 mm transmission lengths (logarithmic scaled). (c) Effect of eccentricity $\|\mathbf{r}\|$ on the relative arm tip twist angle $\mu(\ell)$ for $\beta = 43°$, $\eta = 5.01$ (calibrated), and 12 mm transmission lengths. (d) Effect of eccentricity $\|\mathbf{r}\|$ on the twist angle of distal disk for parameters of (c) and $\theta_1(0) = 90°$. Best viewed in color.

TABLE III
PARAMETERS USED IN SINGLE-STAGE TWO-ARM STABILITY ANALYSIS

	Arm	Backbone
Poisson's ratio	0.33	0.33 (NiTi), 0.42 (polymer)[1]
Curve length (mm)	110	100
Transmission length (mm)	12	0

[1] Polymer backbone was used for case $\eta = 3.51$ to match simulation and experiment.
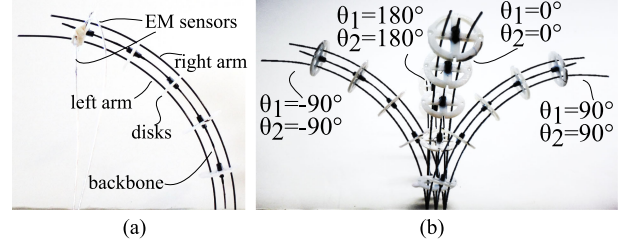

Fig. 11. Single-stage two-arm sheath prototype. Precurved wires are used in place of arm tubes to simply construction. Depicted arm offset from central backbone is 4 mm. (a) Electromagnetic (EM) sensors mounted on distal disk measure position and orientation. (b) Four configurations on workspace boundary.

Table III and three values of $\theta_1(0) \in \{-90°, 0, 90°\}$, model-based computation of the relative channel tube twist angle is plotted in Fig. 9 for three designs. For all curves, the configuration of $\mu(0) = 180°$ was approached using both clockwise and counterclockwise rotations of the second channel tube. Rotation direction for the optimization-based kinematic code refers to the neighboring solution used to initialize the code.

In the first design of Fig. 9(a), the channel tubes possess a precurvature of $\beta = 100°$. The plots for all three values of $\theta_1(0)$ lie on top of each other. Furthermore, the clockwise and counterclockwise solutions produce a unique solution at $\mu(0) = 180°$, which is that $\mu(\ell) = \mu(0) = 180°$. Uniqueness of the input–output mapping indicates that the design is stable.

Fig. 9(b) depicts the case when 17-mm-long transmission lengths have been added to the proximal ends of the channel tubes. As is the case for concentric tube designs, increasing the transmission length tends to destabilize the system. The plot shows that the clockwise and counterclockwise solutions at $\mu(0) = 180°$ are different. This solution multiplicity indicates that the design is unstable and will snap after passing through $\mu(0) = 180°$. The same destabilizing effect can be achieved by increasing the precurvature of the channel tubes, as shown in Fig. 9(c). Here, the precurvature angle has been increased to $\beta = 120°$.

A. Parametric Dependence of Stability

As was shown analytically in [32] and [22], a pair of concentric tubes of equal stiffness and precurvature are stable for precurvature angles less than about $\beta = 79°$. Based on this result, we anticipate that increasing precurvature of channel tubes will also generate instability. In contrast to concentric tube designs, however, channel tube precurvature is reduced during assembly since the central backbone acts to straighten them. Furthermore, a stiffer central backbone will generate a larger reduction in curvature, which is likely to be stabilizing for the assembled design. Consequently, we consider here the effect on stability of both channel tube precurvature and relative stiffness with respect to the central backbone. These can be represented by parameters β for precurvature angle and $\eta = K_{1b}/K_{0b}$ for relative stiffness (channel tube relative to central backbone), respectively. Eccentric tube designs include an additional parameter, namely the offset distance or eccentricity of the channel tubes. Eccentricity can be parameterized by $\|\mathbf{r}\|$, as defined in Fig. 5.

The effect of these three parameters on stability is illustrated in Fig. 10. Simulations were performed using the design given in Table III. Three curves are plotted for the three pairs

$(\theta_1(0), \theta_2(0)) \in \{(-90°, 90°), (0°, 180°), (90°, -90°)\}$. These plots depict only the values of $\mu(\ell)$ corresponding to $\mu(0) = 180°$. If a design is stable, the solution will be $\mu(\ell) = \mu(0) = 180°$ similar to the case of Fig. 9(a). If it is unstable, then the solution will differ from $\mu(\ell) = 180°$, as shown in Fig. 9(b) and (c).

Fig. 10(a) considers the dependence of stability on channel tube precurvature, β. This figure shows that the system is stable for values of $\beta \leq 78°$. As β increases, the three solutions become unstable with the magnitude of relative twist angle varying between solutions.

Fig. 10(b) considers the effect of the relative stiffness of the channel tubes to that of the central backbone, η. Given a precurvature angle of $\beta = 110°$ and a 12 mm transmission length, a concentric tube pair by itself would be unstable. We see, however, that for values of η less than about 0.3, the central backbone stiffness stabilizes the eccentric tube system.

Fig. 10(c) and (d) considers the dependence of stability on eccentricity. Using $\mu(\ell)$ to judge stability in Fig. 10(c), the system appears to be stable for the three cases of $\theta_1(0) \in \{-90°, 0, 90°\}$. If we plot the twist angle of the distal disk, $\theta_0(\ell_0)$, however, we find for the case of $\theta_1(0) = 90°$ that the sheath can twist along its length despite the fact that the arm tubes remain at $\mu(\ell) = \mu(0) = 180°$. Twisting can occur in both positive and negative directions producing an instability for some values of eccentricity $\|\mathbf{r}\|$ as shown in Fig. 10(d).

VII. EXPERIMENTAL VALIDATION

To validate the concept and model, three types of experiments were conducted using two-armed sheath prototypes. The first experiments investigated the stability of a single-stage system to validate the parametric dependence examined in Section VI-A. The second experiments evaluated the kinematic model for a single-stage design while the final experiments evaluated the model for a two-stage sheath.

Prototypes of the single-stage design were constructed, as shown in Fig. 11, with parameters given in Table IV. To simplify construction, precurved NiTi wires were used in place of channel tubes. The central backbones were made from NiTi wire and polymer tubing. The spacer disks were fabricated by 3-D printing with two sets of holes for $\mathbf{r}_i = \{4, 8\}$mm. The disks were 1 mm thick and 18 mm in overall diameter. The clearance between the wires and disk holes was approximately

TABLE IV
PROTOTYPE PARAMETERS OF SINGLE-STAGE ROBOT (CALIBRATED IN BOLD)

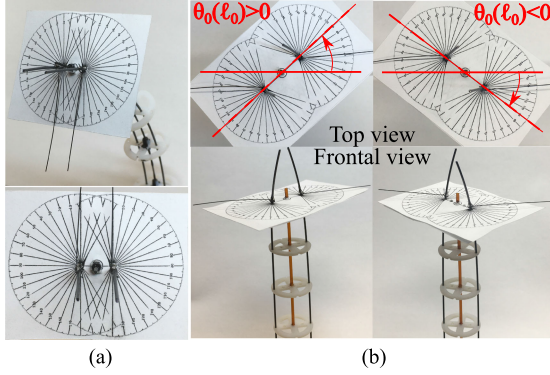|	Arm tube	Backbone
Curve length (mm)	110	100
Outer diameter (mm)	0.762	0.635
Bending stiffness	2.076 (**1.034**)	1
Poisson's ratio	0.33	0.33
Radius of curvature (mm)	85.944	∞

Fig. 12. Elastic stability of single-stage two-arm sheath prototypes. (a) Arm tube twisting is measured with a graduated disk and two twist pointers. (b) Top and front views correspond to case $(\theta_1(0) = 90°, \theta_2(0) = -90°)$. Distal ends of arm tubes remain rotated $180°$ with respect to each other, but the sheath has twisted about its axis. Parameters are $\beta = 43°$, $\nu = 0.42$, $\eta = 5.01$, and $\|\mathbf{r}\| = 8$mm.

0.2 mm. This was found to be the minimum value that allowed free rotation and sliding of the wires with respect to the disks. Larger values produced visible backlash during robot motion.

An electromagnetic (EM) tracking system (3D Guidance trakSTAR, Ascension Co.) was used to record positions and orientations of the base and tip disks as well as rotations of the arm wires. These 6 DOF sensors (Model 180, Ascension Technologies) have the position and orientation precision of 1.4 mm and $0.5°$ rms.

A. Elastic Stability of Single-Stage Sheaths

Elastic stability of single-stage sheaths was investigated experimentally to confirm the parametric dependence observed by simulation in the previous section. The parameters of the prototypes are listed in Table III and were selected to produce experimental data points that could be superimposed on the simulated data of Fig. 10. To measure the relative tip rotation, we mounted a double protractor to the distal end disk, as shown in Fig. 12(a). Two twist pointers were glued to the ends of the arm tubes in order to measure the relative twist angle of the arm tubes. Fig. 12(a) shows the initial setup $\theta_1 = \theta_2 = 0$. Five trials were performed at each configuration. The mean measured relative arm tube twist angles are superimposed in Fig. 10(a)–(c).

While simulated and experimental results are largely in agreement, the experiments in which precurvature angle β was varied revealed some interesting additional behavior. In particular, while the simulations predict two isolated solutions, the experiments revealed that families of "marginally stable" solutions can occur before the system transitions to isolated solutions. These are indicated in Fig. 10(a) by vertical lines connecting

the limiting twist angles. The robot could be moved smoothly through all of these solutions by pushing or twisting its tip. For $\beta = 92°$, all three input configurations exhibited such solution families. For $\beta = 101°$, two of the three input configurations transitioned to snapping between two solutions. At $\beta = 110°$, all three configurations snapped between two solutions. For this value of β, Fig. 10(b) shows the effect of varying stiffness ratio η. As the arm tubes become stiffer relative to the central backbone, instability, as measured by snapping twist angle, increases.

Two experimental values of eccentricity $\|\mathbf{r}\| = \{4, 8\}$mm were compared with simulation results in Fig. 10(c) and (d). As expected, the relative angle between the arm tubes remains equal to $180°$ for both experimental values of eccentricity. Since the double protractor is mounted to the distal disk, it also enabled measurement of central backbone twist relative to the arm tubes, as shown in Fig. 12(b). For the configuration $(\theta_1(0) = 90°, \theta_2(0) = -90°)$, the sheath can be observed from the figure to be straight, but twisted along its axis to $\theta_0(l_0) \approx \pm 45°$ producing two solutions, closely matching the simulated results.

B. Kinematic Calibration of Single-Stage Sheath

The parameters of the design used in these experiments are given in Table IV. For these experiments, base and tip positions and orientations were recorded for a set of 64 uniformly sampled combinations of arm rotation angles. Of the 64 configurations experimentally measured, eight were used for calibration and the remaining 56 were used for assessment.

To compare these measurements to the model, we developed a calibration method using an error performance index J_c, defined based on position and orientation errors between the model and experiment

$$J_c = \sum_{c=1}^{C} \left(\|\mathbf{p}_{c,m} - \mathbf{p}_{c,e}\| + \frac{180}{\pi} \theta(\mathbf{R}_{c,m}^{\mathsf{T}} \mathbf{R}_{c,e}) \right)^2 \qquad (38)$$

where $\mathbf{p}$ and $\mathbf{R}$ denotes the position and rotation matrix of the distal disk, respectively, the subscripts $\cdot_{c,m}$ and $\cdot_{c,m}$ denote the position and orientation from model and experimental data, respectively, of the cth trial out of total C configurations. Also, $\theta(\cdot)$ calculates the rotation angle from the rotation matrix, as defined in [33] and [34]. This choice of the weighting function scales $1°$ of angular error to be equal to 1 mm of position error, as in [35].

The parameters tuned in the calibration were the stiffness ratio of the arms with respect to the central backbone, $\eta = K_{1b}/K_{0b}$, and Poisson's ratio ν of the central backbone and of the arm tubes. The precurvature of the arms was not calibrated since they were shape set in an NC-machined template and were verified to match the template curvature. During calibration, it was observed that adding the disks to the central backbone increased its stiffness from the nominal value.

The calibration process proceeded in two steps. First, the stiffness ratio was calculated using the configurations from the test data in which $\theta_1 = \theta_2$. In these configurations, the arms and central backbone do not experience any twisting and so provide the most direct measurements of relative bending stiffness. After calibrating relative stiffness, Poisson's ratio was calculated.

TABLE V
SHEATH TIP ERROR BEFORE AND AFTER CALIBRATION FOR
SINGLE-STAGE PROTOTYPE

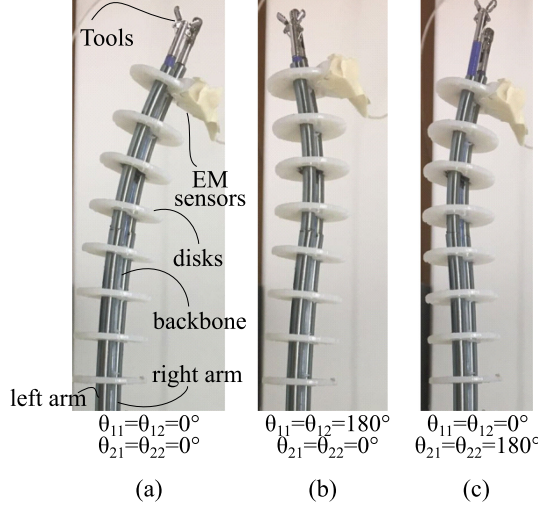|	Position Error (mm)		Angular Error (°)	
	Mean ($\pm$ std)	Maximum	Mean ($\pm$ std)	Maximum
Before Calibration	6.17 ($\pm$2.65)	11.15	5.46 ($\pm$2.22)	10.48
After Calibration	3.60 ($\pm$1.14)	5.39	3.25 ($\pm$1.30)	6.77

Fig. 13. Two-stage two-arm sheath prototype. (a) Curvatures of two stages are aligned. (b) Stage curvatures oppose each other. (c) Labeled components.

TABLE VI
PROTOTYPE PARAMETERS OF TWO-STAGE ROBOT (CALIBRATED IN BOLD)

	Inner tube	Outer tube	Backbone
Curved length (mm)	35	35	-
Straight length (mm)	35	0	65
Transmission length (mm)	5	5	-
Outer diameter (mm)	2.5	2.8	0.762
Inner diameter (mm)	2.2	2.6	-
Bending stiffness	46.38 (**36.13**)	46.77 (**16.16**)	1
Poisson's ratio	0.33	0.33	0.33
Radius of curvature (mm)	83.33	93.33	∞

We found that the calibration of relative bending stiffness produced a significant reduction in the modeling error. In contrast, the error metric J_c was insensitive to variations in Poisson's ratio. The nominal value of $\nu = 0.33$ was effectively optimal.

Position and orientation errors of the distal disk are given in Table V using both the nominal parameter set and the calibrated values. Calibration reduced maximum position error by over 50%. The mean tip position error of 3.6% of robot length is somewhat larger than what has been observed for concentric tube robots, e.g., 2.5% of robot length in [22]. This is likely due to the friction between the arm tubes and the disks, and will depend on disk hole clearance as well as disk thickness in the eccentric tube sheath design. Errors of this size are likely sufficiently small for many applications since they can be compensated for using a feedback loop on the tip position.

C. Kinematic Calibration of Two-Stage Sheath

A two-stage two-arm sheath prototype was built, as shown in Fig. 13. Surgical tools are depicted extending from the arm tubes. The parameters of the design are given in Table VI. Similar to

TABLE VII
SHEATH TIP ERROR BEFORE AND AFTER CALIBRATION FOR
TWO-STAGE PROTOTYPE

	Position Error (mm)		Angular Error (°)	
	Mean ($\pm$ std)	Maximum	Mean ($\pm$ std)	Maximum
Before Calibration	3.68 ($\pm$1.02)	5.93	8.88 ($\pm$2.42)	14.51
After Calibration	1.96 ($\pm$0.92)	4.26	6.70 ($\pm$3.17)	16.1876

the single-stage design, EM sensors have been used to measure poses of base and tip disks for a set of 27 uniformly sampled combinations of inner and outer tubes. The same calibration and error performance index J_c were used as with the single-stage design. The results were similar in that calibration of relative bending stiffness was found to be important, but that error was insensitive to the choice of Poisson's ratio. Table VII shows the position and orientation errors of the distal disk using both nominal and the calibrated values. Calibration reduced mean position error to 53% of the uncalibrated value, which is just 3.0% of robot length.

VIII. CONCLUSION

The development of miniaturized single-port systems incorporating multiple arms delivered through a steerable sheath could significantly expand the number and type of minimally invasive procedures that can be performed in fields like neurosurgery. To address this need, we proposed a steerable sheath technology based on the rotation of eccentrically combined precurved tubes that serve as the working channels for the robotic arms.

While a two-arm sheath actuated using pure rotation was considered here, the work can be extended to consider rotation plus push/pull actuation as well as more arms. For example, a third "arm" could be used for the imaging system and the three actuation tubes would then match the standard number of push/pull tendons.

The initial results presented here are promising and suggest that the approach may provide an effective means of steering multiarmed continuum systems. More work is needed, though, to improve and understand the limits of the approach. In particular, methods for fast kinematic computation are needed and more work is required to characterize the elastic instabilities that may arise.

REFERENCES

[1] B. C. Warf, "Endoscopic third ventriculostomy and choroid plexus cauterization for pediatric hydrocephalus," *Clin. Neurosurg.*, vol. 54, pp. 78–82, 2007.
[2] B. C. Warf, "Comparison of endoscopic third ventriculostomy alone and combined with choroid plexus cauterization in infants younger than 1 year of age: A prospective study in 550 African children," *J. Neurosurg.: Pediatrics*, vol. 103, no. 6, pp. 475–481, 2005.
[3] B. C. Warf, "Hydrocephalus in Uganda: The predominance of infectious origin and primary management with endoscopic third ventriculostomy," *J. Neurosurg.: Pediatrics*, vol. 102, no. 1, pp. 1–15, 2005.
[4] B. C. Warf and J. W. Campbell, "Combined endoscopic third ventriculostomy and choroid plexus cauterization as primary treatment of hydrocephalus for infants with myelomeningocele: Long-term results of a prospective intent-to-treat study in 115 East African infants," *J. Neurosurg.: Pediatrics*, vol. 2, no. 5, pp. 310–316, 2008.

[5] P. Cappabianca *et al.* "Application of neuroendoscopy to intraventricular lesions," *Neurosurgery*, vol. 62, no. suppl_2, pp. SHC 575–SHC598, 2008.

[6] M. L. Apuzzo, W. R. Dobkin, C.-S. Zee, J. C. Chan, S. L. Giannotta, and M. H. Weiss, "Surgical considerations in treatment of intraventricular cysticercosis: An analysis of 45 cases," *J. Neurosurg.*, vol. 60, no. 2, pp. 400–407, 1984.

[7] T. Anor, J. R. Madsen, and P. Dupont, "Algorithms for design of continuum robots using the concentric tubes approach: A. neurosurgical example," in *Proc. IEEE Int. Conf. Robot. Autom.*, 2011, pp. 667–673.

[8] M. R. Gaab and H. W. Schroeder, "Neuroendoscopic approach to intraventricular lesions," *J. Neurosurg.*, vol. 88, no. 3, pp. 496–505, 1998.

[9] K. Oka, M. Yamamoto, S. Nagasaka, and M. Tomonaga, "Endoneurosurgical treatment for hydrocephalus caused by intraventricular tumors," *Child's Nervous Syst.*, vol. 10, no. 3, pp. 162–166, 1994.

[10] B. Bahuleyan, S. Manjila, S. Robinson, and A. R. Cohen, "Minimally invasive endoscopic transventricular hemispherotomy for medically intractable epilepsy: A new approach and cadaveric demonstration," *J. Neurosurg.: Pediatrics*, vol. 6, no. 6, pp. 536–540, 2010.

[11] M. M. Souweidane, "Endoscopic surgery for intraventricular brain tumors in patients without hydrocephalus," *Operative Neurosurg.*, vol. 57, no. suppl_4, pp. ONS– 312, 2005.

[12] B. Badie, N. Brooks, and M. M. Souweidane, "Endoscopic and minimally invasive microsurgical approaches for treating brain tumor patients," *J. Neuro-oncol.*, vol. 69, no. 1–3, pp. 209–219, 2004.

[13] B. P. M. Yeung and T. Gourlay, "A technical review of flexible endoscopic multitasking platforms," *Int. J. Surg.*, vol. 10, no. 7, pp. 345–354, 2012.

[14] J. Burgner *et al.*, "A telerobotic system for transnasal surgery," *IEEE/ASME Trans. Mechatron.*, vol. 19, no. 3, pp. 996–1006, Jun. 2014.

[15] M. T. Chikhaoui, J. Granna, J. Starke, and J. Burgner-Kahrs, "Toward motion coordination control and design optimization for dual-arm concentric tube continuum robots," *IEEE Robot. Autom. Lett.*, vol. 3, no. 3, pp. 1793–1800, Jul. 2018.

[16] D. B. Camarillo, C. R. Carlson, and J. K. Salisbury, "Configuration tracking for continuum manipulators with coupled tendon drive," *IEEE Trans. Robot.*, vol. 25, no. 4, pp. 798–808, Aug. 2009.

[17] A. Bajo, R. B. Pickens, S. D. Herrell, and N. Simaan, "Constrained motion control of multisegment continuum robots for transurethral bladder resection and surveillance," in *Proc. IEEE Int. Conf. Robot. Autom.*, May 2013, pp. 5837–5842.

[18] R. E. Goldman, A. Bajo, L. S. MacLachlan, R. Pickens, S. D. Herrell, and N. Simaan, "Design and performance evaluation of a minimally invasive telerobotic platform for transurethral surveillance and intervention," *IEEE Trans. Biomed. Eng.*, vol. 60, no. 4, pp. 918–925, Apr. 2013.

[19] N. Sarli, G. Del Giudice, S. De, M. S. Dietrich, S. D. Herrell, and N. Simaan, "Preliminary porcine in vivo evaluation of a telerobotic system for transurethral bladder tumor resection and surveillance," *J. Endourol.*, vol. 32, no. 6, pp. 516–522, 2018.

[20] B. Kang, R. Kojcev, and E. Sinibaldi, "The first interlaced continuum robot, devised to intrinsically follow the leader," *PLOS One*, vol. 11, no. 2, Feb. 2016, Art no. e0 150278.

[21] A. Degani, H. Choset, A. Wolf, and M. A. Zenati, "Highly articulated robotic probe for minimally invasive surgery," in *Proc. IEEE Int. Conf. Robot. Autom.*, May 2006, pp. 4167–4172.

[22] P. E. Dupont, J. Lock, B. Itkowitz, and E. Butler, "Design and control of concentric-tube robots," *IEEE Trans. Robot.*, vol. 26, no. 2, pp. 209–225, Apr. 2010.

[23] H. Yu, L. Wu, K. Wu, and H. Ren, "Development of a multi-channel concentric tube robotic system with active vision for transnasal nasopharyngeal carcinoma procedures," *IEEE Robot. Autom. Lett.*, vol. 1, no. 2, pp. 1172–1178, Jul. 2016.

[24] Z. Mitros, M. Khadem, C. Seneci, S. Ourselin, L. Da Cruz, and C. Bergeles, "Towards modelling multi-arm robots: Eccentric arrangement of concentric tubes," in *Proc. 7th IEEE Int. Conf. Biomed. Robot. Biomechatronics*, 2018, pp. 43–48.

[25] D. C. Rucker, I. R.J.G. S. Webster Chirikjian, and N. J. Cowan, "Equilibrium conformations of concentric-tube continuum robots," *Int. J. Robot. Res.*, vol. 29, no. 10, pp. 1263–1280, 2010.

[26] J. Wang, J. Ha, and P. E. Dupont, "Steering a multi-armed robotic sheath using eccentric precurved tubes," in *Proc. Int. Conf. Robot. Autom.*, May 2019, pp. 9834–9840.

[27] P. Sears and P. Dupont, "A steerable needle technology using curved concentric tubes," in *Proc. IEEE/RSJ Int. Conf. Intell. Robots Syst.*, 2006, pp. 2850–2856.

[28] K. Xu and N. Simaan, "Analytic formulation for kinematics, statics, and shape restoration of multibackbone continuum robots via elliptic integrals," *J. Mechanisms Robot.*, vol. 2, no. 1, 2010, Art no. 0 11006.

[29] C. B. Black, J. Till, and D. C. Rucker, "Parallel continuum robots: Modeling, analysis, and actuation-based force sensing," *IEEE Trans. Robot.*, vol. 34, no. 1, pp. 29–47, Feb. 2018.

[30] M. Mahvash and P. E. Dupont, "Stiffness control of surgical continuum manipulators," *IEEE Trans. Robot.*, vol. 27, no. 2, pp. 334–345, Apr. 2011.

[31] J. Lock, G. Laing, M. Mahvash, and P. E. Dupont, "Quasistatic modeling of concentric tube robots with external loads," in *Proc. IEEE/RSJ Int. Conf. Intell. Robots Syst.*, 2010, pp. 2325–2332.

[32] J. Ha, F. C. Park, and P. E. Dupont, "Optimizing tube precurvature to enhance the elastic stability of concentric tube robots," *IEEE Trans. Robot.*, vol. 33, no. 1, pp. 22–37, Feb. 2017.

[33] J. Wang, L. Wu, M. Q. . Meng, and H. Ren, "Towards simultaneous coordinate calibrations for cooperative multiple robots," in *Proc. IEEE/RSJ Int. Conf. Intell. Robots Syst.*, 2014, pp. 410–415.

[34] L. Wu *et al.*, "Simultaneous hand-eye, tool-flange, and robot-robot calibration for comanipulation by solving the AXB=YCZ problem," *IEEE Trans. Robot.*, vol. 32, no. 2, pp. 413–428, Apr. 2016.

[35] J. Ha, G. Fagogenis, and P. E. Dupont, "Modeling tube clearance and bounding the effect of friction in concentric tube robot kinematics," *IEEE Trans. Robot.*, vol. 35, no. 2, pp. 353–370, Apr. 2019.

Jiaole Wang (Member, IEEE) received the B.E. degree in mechanical engineering from the Beijing Information Science and Technology University, Beijing, China, in 2007, the M.E. degree from the Department of Human and Artificial Intelligent Systems, University of Fukui, Fukui, Japan, in 2010, and the Ph.D. degree from the Department of Electronic Engineering, The Chinese University of Hong Kong, Hong Kong, in 2016.

He was a Research Fellow with Pediatric Cardiac Bioengineering Laboratory, Department of Cardiovascular Surgery, Boston Children's Hospital, Harvard Medical School, Boston, MA, USA. He is currently an Associate Professor with the School of Mechanical Engineering and Automation, Harbin Institute of Technology, Shenzhen, China. His main research interests include medical and surgical robotics, image-guided surgery, human–robot interaction, and magnetic tracking and actuation for biomedical applications.

Joseph Peine received the B.S. and M.S. degrees in mechanical engineering from Johns Hopkins University, Baltimore, MD, USA, in 2017 and 2018, respectively.

He is currently a Medical Device Engineer with Pediatric Cardiac Bioengineering Laboratory, Department of Cardiovascular Surgery, Boston Children's Hospital, Harvard Medical School, Boston, MA, USA. His main research interests include medical devices and surgical robotics.

Pierre E. Dupont (Fellow, IEEE) received the B.S., M.S., and Ph.D. degrees in mechanical engineering from Rensselaer Polytechnic Institute, Troy, NY, USA, in 1982, 1984, and 1988, respectively.

From 1988 to 1990, he was a Postdoctoral Fellow with the School of Engineering and Applied Sciences, Harvard University, Cambridge, MA, USA. He was a Professor of Mechanical Engineering and Biomedical Engineering with Boston University, Boston, MA, USA. He is currently the Chief of Pediatric Cardiac Bioengineering and holder of the Edward P. Marram Chair at Boston Children's Hospital, Harvard Medical School, Boston, MA, USA. He is also a Professor of Surgery with Harvard Medical School, Boston. His research group develops robotic instrumentation and imaging technology for medical applications.

Dr. Dupont just completed a 5-year term as a Senior Editor for the IEEE TRANSACTIONS ON ROBOTICS and is currently a member of the Advisory Board for *Science Robotics*.